Characterization and Modulation of Langmuir Circulation in Chesapeake Bay

MALCOLM E. SCULLY

Applied Ocean Physics and Engineering Department, Woods Hole Oceanographic Institution, Woods Hole, Massachusetts

ALEXANDER W. FISHER, STEVEN E. SUTTLES, LAWRENCE P. SANFORD, AND WILLIAM C. BOICOURT

University of Maryland Center for Environmental Science, Horn Point Laboratory, Cambridge, Maryland

(Manuscript received 1 December 2014, in final form 16 July 2015)

ABSTRACT

Measurements made as part of a large-scale experiment to examine wind-driven circulation and mixing in Chesapeake Bay demonstrate that circulations consistent with Langmuir circulation play an important role in surface boundary layer dynamics. Under conditions when the turbulent Langmuir number La_t is low (<0.5), the surface mixed layer is characterized by 1) elevated vertical turbulent kinetic energy; 2) decreased anisotropy; 3) negative vertical velocity skewness indicative of strong/narrow downwelling and weak/broad upwelling; and 4) strong negative correlations between low-frequency vertical velocity and the velocity in the direction of wave propagation. These characteristics appear to be primarily the result of the vortex force associated with the surface wave field, but convection driven by a destabilizing heat flux is observed and appears to contribute significantly to the observed negative vertical velocity skewness.

Conditions that favor convection usually also have strong Langmuir forcing, and these two processes probably both contribute to the surface mixed layer turbulence. Conditions in which traditional stress-driven turbulence is important are limited in this dataset. Unlike other shallow coastal systems where full water column Langmuir circulation has been observed, the salinity stratification in Chesapeake Bay is nearly always strong enough to prevent full-depth circulation from developing.

1. Introduction

There is considerable evidence that the presence of Langmuir circulation (LC) fundamentally alters the dynamics of the surface boundary layer in the ocean (Weller and Price 1988; Li and Garrett 1997; Kukulka et al. 2010; Belcher et al. 2012). Various mechanisms have been proposed for the formation of LC, but the most widely accepted explanation is that the wave-driven Stokes drift tilts vertical vorticity into the streamwise direction, leading to coherent vortices that are aligned with the direction of wave propagation (Craik and Leibovich 1976). The Craik–Leibovich (CL) vortex force has been incorporated into large-eddy simulations (LES), which have simulated coherent wind-aligned vortices that are largely consistent with field observations of LC (Skyllingstad and Denbo 1995; McWilliams et al. 1997; Noh et al. 2004; Polton and Belcher 2007). Most observational studies have been conducted in deep water, where bottom boundary layer turbulence has no influence on the surface layer dynamics (Weller et al. 1985; Weller and Price 1988; Zedel and Farmer 1991; Smith 1992; Plueddemann et al. 1996). A notable exception was the comprehensive measurements collected on the New Jersey continental shelf, where an acoustic Doppler current profiler (ADCP) with a fifth vertical beam was deployed in ~15 m of water (Gargett et al. 2004; Gargett and Wells 2007). This study documented Langmuir supercells (LSCs), a term coined to describe circulations that spanned the entire water column. Unlike observations made in deeper water, the observations of Gargett and Wells (2007) show that the presence of the bottom boundary led to an intensified near-bed downwind jet under the downwelling regions. LES that include a bottom boundary layer in shallow water suggests that LC fundamentally alters the near-bed turbulence and disrupts the classically assumed log layer (Tejada-Martinez et al. 2012).

Corresponding author address: Malcolm E. Scully, Applied Ocean Physics and Engineering Department, Woods Hole Oceanographic Institution, MS 10, Woods Hole, MA 02543.
E-mail: mscully@whoi.edu

DOI: 10.1175/JPO-D-14-0239.1

While these studies show how LC can impact the dynamics of the bottom boundary layer, bottom-generated turbulence also might alter or prevent the formation of LC in shallow coastal waters. Gargett and Wells (2007) suggest that bottom-generated turbulence can disrupt LC in shallow environments when tidal currents become large. Kukulka et al. (2011) used a combination of observations and LES to demonstrate how crosswind tidal shear distorts and disrupts LC in the coastal ocean. Their simple scaling clearly shows that significant distortion/disruption of LC occurs when the advective time scale associated with the shear is short compared to the turnover time scale of the LC. In contrast to open-ocean currents, waves and currents in enclosed coastal environments are not often aligned. Yet, most of the LES of LC have considered conditions where the wind, waves, and currents are aligned. For conditions where the mean current direction is opposed to the direction of wave propagation, theory suggests that the vortex force would be stabilizing, preventing the formation of LC (Leibovich 1983).

In addition to the enhanced shear caused by the presence of the bottom boundary layer, estuarine and coastal environments also typically experience stronger vertical density stratification as compared to open-ocean environments because of the input of freshwater. The presence of strong stratification is thought to inhibit the formation of LC (Leibovich and Paolucci 1981; Phillips 2001). However, there is evidence that LC can accelerate the deepening of the surface mixed layer (Kukulka et al. 2010). This deepening by LC is thought to occur via two primary mechanisms: 1) engulfing stratified water into the mixed layer via LC and 2) shear instability driven by enhanced shear under downwelling regions of LC (Li and Garrett 1997). Li and Garrett (1997) suggest that engulfment by LC dominates when the velocity difference at the base of the surface mixed layer is small, while Kukulka et al. (2010) conclude that the LC-enhanced shear at the base of the mixed layer is more important.

Given the presence of both strong stratification and persistent tidal shear, we do not expect LC to play an important role in the surface mixed layer process in estuarine environments. However, as we will demonstrate in this paper, strong coherent circulations consistent with LC are observed in Chesapeake Bay and, when present, dominate the mixing in the surface mixed layer. The goal of this paper is to present a comprehensive description and characterization of LC in Chesapeake Bay. Section 2 provides an overview of an experiment that was conducted in the fall of 2013 and the basic analysis that was conducted. Section 3 presents the results, including a detailed characterization of the observed circulation, its consistency with LC, and how stratification, surface heat flux, and tidal currents modify the observed circulation. The results are discussed in section 4, where we discuss that both LC and convection contribute to observed turbulence characteristics of the surface mixed layer.

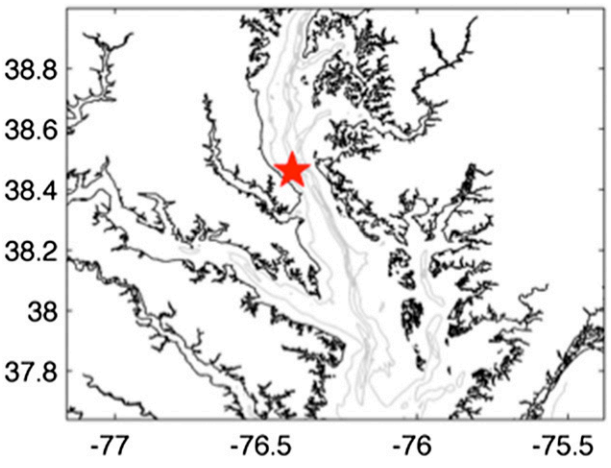

FIG. 1. Site map showing the location of instrumented turbulence tower at a depth of approximately 14 m in Chesapeake Bay, United States.

2. Methods

a. *Fall 2013 Chesapeake Bay Experiment*

The observations presented in this paper were collected as part of a collaborative research project to examine wind-driven circulation and mixing in Chesapeake Bay during the fall of 2013. During this project water column moorings, bottom landers, and surface meteorological buoys were maintained in the central region of Chesapeake Bay during the spring of 2012 and fall of 2013. The results presented below focus primarily on an instrumented turbulence tower that was deployed along the broad western shoal in 14 m of water (Fig. 1) during fall 2013. The tower was ~1.5 km from the western shoreline in a region where the bathymetry is relatively constant. The tower deployed in this study is similar to guyed communication towers, with a triangular cross section reinforced with a lattice of cross braces (Fig. 2). The tower sits atop a universal joint that is affixed to a base plate that sits on the seafloor. The tower is held rigidly upright by four guy wires that attach to the top of the tower at one end and are secured to four anchors (1000-lb railroad wheels) at the other. Winches attached to the top of the tower are used to tighten the guy wires and ensure that the tower is vertical and rigid. An instrumented platform is located at the top of the tower, which sits above the water surface by 2 m.

Six Nortek vector acoustic Doppler velocimeters (ADVs) were arrayed vertically at 2-m intervals along

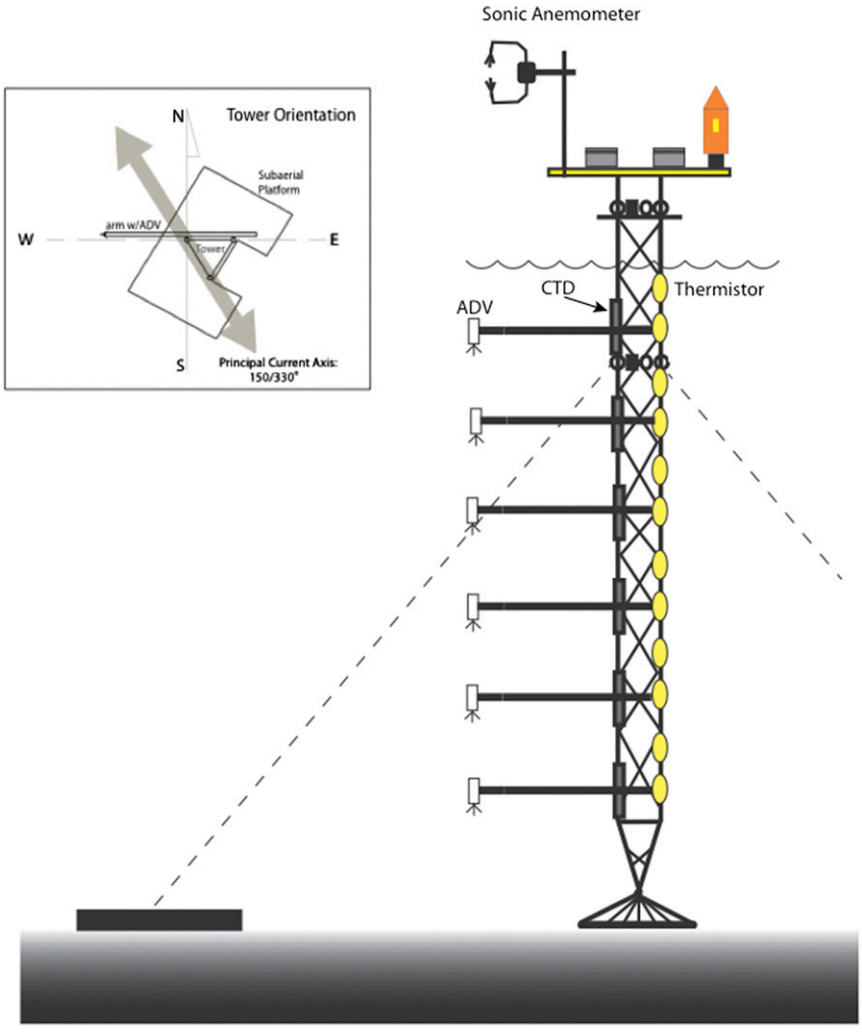

FIG. 2. Schematic of the turbulence tower, showing the locations of the 6 ADVs, 6 CTDs, 12 thermistors, and the sonic anemometer. Inset shows the tower orientation relative to principal tidal current axis.

the tower, beginning approximately 1.5 m from the mean water surface. The ADV sensor heads were mounted in a downward-looking orientation at the end of 1-m poles that were aligned perpendicular to along-channel tidal flow (see Fig. 2). The ADVs sampled at 32 Hz and collected 28 min of data every half hour yielding nearly continuous velocity and pressure data. In addition to the ADVs, the tower contained six Seabird SBE37 MicroCAT CTDs with dissolved oxygen sensors that sampled every 5 min. The CTDs were mounted to the tower and aligned with the ADV sampling volumes providing estimates of the vertical density structure throughout the experiment. A vertical array of 12 RBR solo-T thermistors also was deployed along the vertical extent of the tower, measuring temperature at 1 Hz with a vertical spacing of 1 m. The uppermost and lowermost thermistors were 1.3 and 12.5 m from the mean water surface, respectively. The tower was deployed on 18 September 2013 and recovered on 29 October 2013. The batteries for the top two ADVs were exhausted on 18 October, so our analysis will focus on the 1-month period when data from all six ADVs is available.

A Campbell Scientific Open Path Eddy Covariance System (OPEC) was deployed on the subaerial platform at the top of the tower and consisted of a 3D sonic anemometer (CSAT3) and a type E fine-wire thermocouple (FW05). The system sampled the three-dimensional velocity field and air temperature at 10 Hz continuously, and the sampling volume of the sonic anemometer was located at ~2.82 m above the mean water surface. For this analysis, we chose to simply use the bulk fluxes (Fairall et al. 1996) to calculate the surface fluxes of heat and momentum (see below). A detailed comparison between the direct covariance fluxes and the

bulk formulations demonstrates agreement to within ±20% (Fisher et al. 2015).

Located 60 m northwest of the tower was a bottom lander with an upward-looking 1200-kHz RDI ADCP, a Nortek vector ADV, and Seabird SBE37 MicroCAT CTD with dissolved oxygen sensor. For the data presented below, the ADCP pinged at 1 Hz for 30 s and recorded a current profiles with 1-m vertical resolution every 30 s. The bottom-mounted ADV sampled at 32 Hz for 28 min every half hour and the SBE37 sampled every 5 min.

b. Analysis

The primary focus of this study is the vertical array of ADVs deployed on the tower. The orientation of poles on which the ADVs were mounted was due west (270°), while the channel orientation in this region of the bay is 150°–330° (Fig. 2). As a result, flows from the east–southeast could produce wakes off the tower that could contaminate our observations. To prevent these flows from influencing our interpretation of the data, any flows from 70° to 130° are excluded from our quantitative analysis. These data are not excluded from several figures of a more qualitative nature, but we are confident that the interpretation of these figures is not influenced by the presence of the tower. Unless otherwise noted, the velocity data are rotated into an along-wave coordinate system based on the dominant wave direction where u, v, and w represent the along-wave, across-wave, and vertical velocities, respectively. We use a right-hand coordinate system where positive u is downwave, positive v is to the left of the direction of wave propagation, and positive w is upward.

A primary goal of this paper is to identify and quantity the motions associated with LC in Chesapeake Bay. One way this will be done is through estimates of the turbulent velocity variances ($\sigma_u^2, \sigma_v^2,$ and σ_w^2). Calculation of the turbulent velocity variance is not straightforward because of the presence of nonturbulent motions induced by surface gravity waves. Near the ocean surface, wave orbital motions can be an order of magnitude greater than turbulent fluctuations, making direct measurements of turbulent motions difficult. To address this difficulty, we employ the spectral fitting techniques outlined in Gerbi et al. (2009). For clarity, we briefly summarize these methods here. Because of the differences in the noise floor for the horizontal and vertical components of velocity measured by an ADV (Voulgaris and Trowbridge 1998), different methods are used for the horizontal and vertical variances. For the vertical component of velocity, we fit the spectral model of Kaimal et al. (1972) using a two-parameter least squares minimization. The fitting procedure omits all the spectral energy within the wave band (1/8 to 1 Hz) and all spectral energy higher than twice the noise floor. The energy at frequencies higher than the wave band is adjusted downward to account for the effect of unsteady advection by waves following the model of Lumley and Terray (1983), including all three components of wave orbital motion, as outlined in Gerbi et al. (2009). The higher noise floor for the horizontal components of velocity often completely obscures the inertial subrange, so only the low-frequency (<1/8 Hz) portion of the spectra is used in the fitting procedure, and we assume that higher frequencies asymptote to an isotropic inertial subrange that matches the vertical component of velocity. From the estimates of the turbulent velocity variance, the turbulent kinetic energy (TKE) is defined as $q^2 = 1/2(\sigma_u^2, \sigma_v^2, \sigma_w^2)$.

Measurements of σ_w^2 in the ocean's surface boundary layer are typically larger than comparable measurement made near a fixed boundary. D'Asaro (2001) and Tseng and D'Asaro (2004) found values of σ_w^2/u_*^2 (where u_* is the surface friction velocity) that were up to twice the values from laboratory and bottom boundary layer measurements. Elevated σ_w^2 in the surface boundary layer has been attributed to both LC and wave breaking. The degree of anisotropy of the turbulence also has been used as a diagnostic for LC (McWilliams et al. 1997; Teixeira and Belcher 2002; Polton and Belcher 2007). For flow near a rigid boundary, the mean shear enhances σ_u^2 and the proximity to the boundary limits σ_w^2, resulting in anisotropy where $\sigma_u^2 > \sigma_v^2 > \sigma_w^2$. In contrast, LES suggests that the presence of LC enhances σ_w^2 and σ_v^2 relative to σ_u^2, resulting in $\sigma_w^2 > \sigma_v^2 > \sigma_u^2$ (Polton and Belcher 2007). Field observations of LSCs from a shallow and unstratified continental shelf demonstrate an intensified downwind jet characterized by enhanced σ_u^2 near the bed (Gargett et al. 2004; Gargett and Wells 2007). Consistent with previous observations and LES, we will use both the intensity of vertical velocity variance (σ_w^2/u_*^2), as well as the overall anisotropy (σ_u^2/q, σ_v^2/q and σ_w^2/q), to characterize the turbulence and infer the presence of LC.

In addition to quantifying the turbulent velocity variance, the ADV velocity data are used to quantify the coherence of the observed low-frequency motions and infer some basic properties of the flow. One metric we use to characterize the observed circulation is the vertical velocity skewness defined as

$$\gamma = \frac{\overline{\langle w \rangle^3}}{\overline{\langle w \rangle^2}^{3/2}}, \tag{1}$$

where the angled brackets indicate that the vertical velocity for each burst has been low-pass filtered with a

cutoff frequency of 1/20 Hz and linearly detrended (effectively bandpass filtering the data), and the overbar represents a burst average. LC, which typically has stronger and narrower downwelling and weaker and wider upwelling, has been shown to exhibit negative values of γ in LES (McWilliams et al. 1997; Sullivan et al. 2007). Calculating γ using the filtered data is comparable to LES studies, which do not resolve individual wave motions. A commonly noted characteristic of LC is the presence of an intensified downwind jet associated with the convergent downwelling regions and a corresponding negative velocity perturbation in the along-wind direction associated with the upwelling regions. The tower data were collected at a fixed vertical location and do not provide any direct information about the orientation of LC. However, if we assume that the downwind jet coincides with downwelling regions, we can infer the orientation of the surface convergence by finding the rotation angle that minimizes (i.e., most negative) the correlation over the 28-min burst between the low-frequency (<1/20 Hz) horizontal and vertical velocities. The orientation of the observed circulation cell inferred from this analysis is denoted as θ_{cell}, and the correlation after rotation is denoted as $r_{\min}$; we will use a metric to quantify the overall coherence of the low-frequency motions.

The metrics presented above provide the framework for characterizing the observed turbulence. To estimate the overall strength of LC forcing, we use the turbulent Langmuir number, given as

$$\mathrm{La}_t = \left(\frac{u_*}{U_S}\right)^{1/2}, \tag{2}$$

where U_S is the surface value of the Stokes drift velocity. Values of u_* were estimated from the bulk flux formulations (Fairall et al. 1996) using the wind speed measured at the tower. For a turbulent surface mixed layer, La_t represents the competition between shear instability driven by the surface wind forcing and the vortex force driven by LC. In the open ocean, La_t is typically 0.2–0.5 for equilibrium waves (McWilliams et al. 1997), but higher values have been found in coastal environments that exhibit LC (Gargett and Wells 2007; Belcher et al. 2012). In shallow coastal environments, bottom-generated turbulence has been shown to impact LC (e.g., Tejada-Martinez et al. 2012). Gargett and Grosch (2014) define a bottom Langmuir number La_H that represents the ratio of the bottom stress velocity u_{*b} to the Stokes drift forcing, defined as

$$\mathrm{La}_H = \frac{u_{*b}}{U_S}. \tag{3}$$

For simplicity, u_{*b} is estimated from the velocity measured by the ADV 0.88 m above the bed and a constant drag coefficient (0.002). Gargett and Grosch (2014) suggest that bottom-generated turbulence is important when $\mathrm{La}_H > 2\mathrm{La}_t^2$.

Given the importance of the Stokes drift to LC, a number of studies (Min and Noh 2004; Grant and Belcher 2009; Harcourt and D'Asaro 2008) have suggested that the appropriate scaling for Langmuir turbulence is

$$u_{*\mathrm{LC}} = U_S^{1/3} u_*^{2/3}. \tag{4}$$

When there is sufficient heat loss through the ocean surface, convective instability contributes to surface turbulence (e.g., Shay and Gregg 1986) and the surface buoyancy flux can provide the dominant source of energy for turbulent exchange. Under conditions of strong surface heat loss, the expected velocity scale for turbulent motions becomes

$$w_* = (B_0 H_m)^{1/3} = \left(\frac{Q\alpha g H_m}{C_\rho \rho_0}\right)^{1/3}, \tag{5}$$

where H_m is the surface mixed layer depth, and B_0 is the surface buoyance flux, which is estimated from the net surface heat flux Q (positive for heat gain by the ocean). In calculating B_0, α is the coefficient of thermal expansion ($\sim 2.3 \times 10^{-4}\,^\circ\mathrm{C}^{-1}$), g is the gravitational acceleration, C_ρ is the specific heat of water ($4100\,\mathrm{J\,kg^{-1}\,^\circ C^{-1}}$), and ρ_0 is the reference density of seawater ($1008\,\mathrm{kg\,m^{-3}}$). Rayleigh–Bénard convective instabilities have many of the same qualitative features of LC, including coherent structures characterized by narrower, stronger downwelling and broader, weaker upwelling. To try and identify the dominant forcing mechanism, we calculate the ratio of the buoyancy forcing that drives thermal convection to the vortex force that drives LC, which can be represented as the Hoenikker number (Li and Garrett 1995):

$$\mathrm{Ho} = \frac{-2\alpha g Q}{\rho_0 C_\rho k U_S u_*^2} = \frac{-2w_*^3}{u_{*\mathrm{LC}}^3 k H_m}, \tag{6}$$

where k is the wavenumber of the dominant surface waves. Values of Ho are negative under stabilizing heat flux and positive for destabilizing heat flux. It has been suggested that for conditions where $\mathrm{Ho} < -1$, LC is shut down by the near-surface stratification induced by surface heating (Min and Noh 2004). Similarly, values of $\mathrm{Ho} > 1$ have been suggested to mark the transition to buoyancy-dominated turbulence (McWilliams et al. 1997).

Estimates of Q require the net shortwave radiation Q_s, net longwave radiation Q_b, sensible heat flux Q_h, and latent heat flux Q_e. The Q_h and Q_e are estimated from the bulk fluxes (Fairall et al. 1996) using the observed wind speed, surface water temperature, air temperature, and relative humidity at the tower. Neither Q_s nor Q_b were measured, so we obtained estimates of these terms from the NCEP North American Regional Reanalysis model for the model location closest to central Chesapeake Bay.

Unlike the open ocean where the surface heat flux generally is the dominant source of buoyancy, the stability of the water column in estuarine and coastal environments usually is dominated by vertical salinity gradients associated with freshwater inputs. Therefore, it is useful to quantify the impact of water column stability based on the local stratification and not the surface heat flux. Li and Garrett (1997) suggested that the deepening of the surface mixed layer due to LC was arrested when

$$\Delta b \geq C \frac{u_*^2}{H_m}, \tag{7}$$

where Δb is the buoyancy jump ($\Delta b = g' = g\Delta\rho/\rho_0$) at the base of a surface mixed layer of depth H_m, and C is a coefficient that depends on sea state, with $C \sim 50$ for fully developed seas. We use this relationship to define H_m by finding the shallowest depth along the tower where this criteria is satisfied, using $C \sim 50$ for simplicity. If none of the observed values of Δb estimated from adjacent CTDs on the tower exceed this limit, we assume H_m is the full water depth H. For conditions when $H_m < H$, we assume the stratification is sufficient to prevent full water column LC from developing.

Significant wave height H_s, peak wave period T, and dominant wave direction Θ are derived from the directional wave spectra $E_{\eta\eta}$, calculated from the uppermost ADV on the tower ($z \sim 1.5$ m). Estimates of $E_{\eta\eta}$ are calculated using all three components of velocity and pressure using the maximum likelihood method (IMLM) (Pawka 1983; Johnson 2002). The surface value of the Stokes drift U_S in the direction of primary wave propagation is calculated from the directional wave spectrum following Kenyon (1969):

$$U_S = \int_0^{2\pi} \int_0^{\hat{\omega}_{\max}} E_{\eta\eta} \hat{\omega} k \frac{\cosh(2kH)}{\sinh^2(kH)} \cos(\theta - \Theta)\, \partial\hat{\omega}\, \partial\theta, \tag{8}$$

where k is the radian wavenumber, θ is wave direction, and $\hat{\omega}$ is the wave frequency, which has been adjusted to account for Doppler shifting by the mean currents following the methods of Jones and Monismith (2007), where

$$\omega = \hat{\omega} + U\cos(\theta - \phi), \tag{9}$$

where ω is the observed frequency, and ϕ is the mean current U direction. The Doppler shift correction only had a modest (<10%) impact on the calculated values of U_S. Because of the noise limitations of the ADV, the directional wave spectra above 0.6 Hz are not reliable (Jones and Monismith 2007). In addition, the uppermost ADV was ~1.5 m from the surface, so motions associated with high-frequency waves were attenuated at this depth. Therefore, in calculating U_S we extended the spectra to higher frequencies by appending a ω^{-4} tail (Kitaigorodskii 1983). As with the Doppler shift correction, this procedure had only a minor impact on the calculated values. Values of U_S calculated from H_s and the peak frequency were ~20% larger than calculated via Eq. (8), presumably because this method does not account for directional spreading.

3. Results

a. Overview of experiment

The results in this paper will focus on the period of Julian day (JD) 263–293 when nearly continuous ADV data are available from all six sensors. This period is characterized by several energetic wind events, with sustained wind speeds in excess of 7–8 m s^{-1} (Fig. 3). The most notable event during the period was JD 280–287 when winds were approximately 10 m s^{-1} for nearly a week (Fig. 3a). During this period, low pressure was centered off the coast, and moderately strong winds from the northeast persisted at our study site. Wind speed and wave height are highly correlated in this fetch-limited system, with essentially no nonlocal swell. Significant wave height exceeded 1.0 m during the sustained nor'easter, with dominant wave periods of 4 s (Figs. 3b,c). The mean water temperature cooled significantly during this period, with the greatest decrease in temperature coming during the period of prolonged northeast winds, consistent with heat loss to the atmosphere (Fig. 3d). There was a period of positive heat flux between 1 and 7 October, prior to the nor'easter, when winds were generally weak and from the southwest and air temperatures were warmer than average. During the nor'easter, there was significant heat loss and a corresponding drop in mean water temperature. Estimates of Q show significant diurnal variability throughout the period, with maximum values occurring midday, consistent with the daily variability of incoming solar radiation. Thus, with the exception of the nor'easter in early October, the surface heat flux changes sign at diurnal time scales, with an overall range of ±400 W m^{-2} (Fig. 3e).

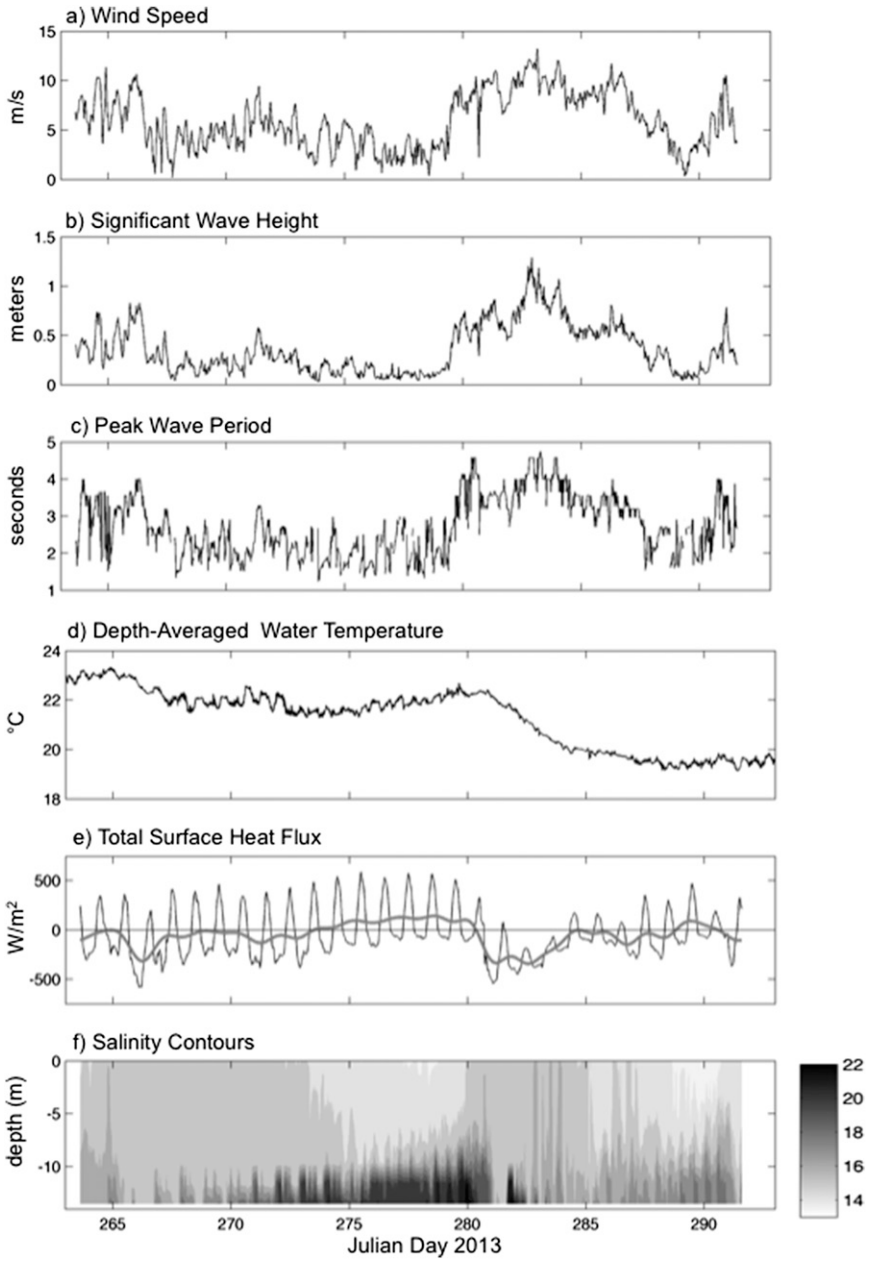

FIG. 3. Overview of conditions during the 2013 experiment including (a) 10-m neutral wind speed ($m\,s^{-1}$) measured at the tower; (b) significant wave height (m) estimated from surface ADV; (c) peak wave period (s) estimated from surface ADV; (d) depth-averaged water temperature (°C) from the vertical array of 12 thermistors; (e) estimated total surface heat flux ($W\,m^{-2}$) (thin line), with 35-h low-pass data (thick gray line); and (f) contours of salinity (psu) from the six CTDs on tower combined with bottom salinity from the adjacent bottom lander and surface salinity from adjacent buoy (contour interval is 1 psu).

Weak-to-moderate salinity stratification persisted in the lower half of the water column throughout the experiment, with a few brief periods when the water column became totally well mixed (Fig. 3f). Despite the near-bed stratification, the upper portion of the water column was typically well mixed with respect to salinity down to a depth of about 10 m under strong forcing. Estimates of La_t were below 0.5 for 40% the experiment, including the majority of the prolonged northeast wind event (Fig. 4a). The magnitude of Ho is strongly correlated with La_t, and conditions with $La_t < 0.5$ generally correspond to $|Ho| < 0.1$, suggesting a dominance of

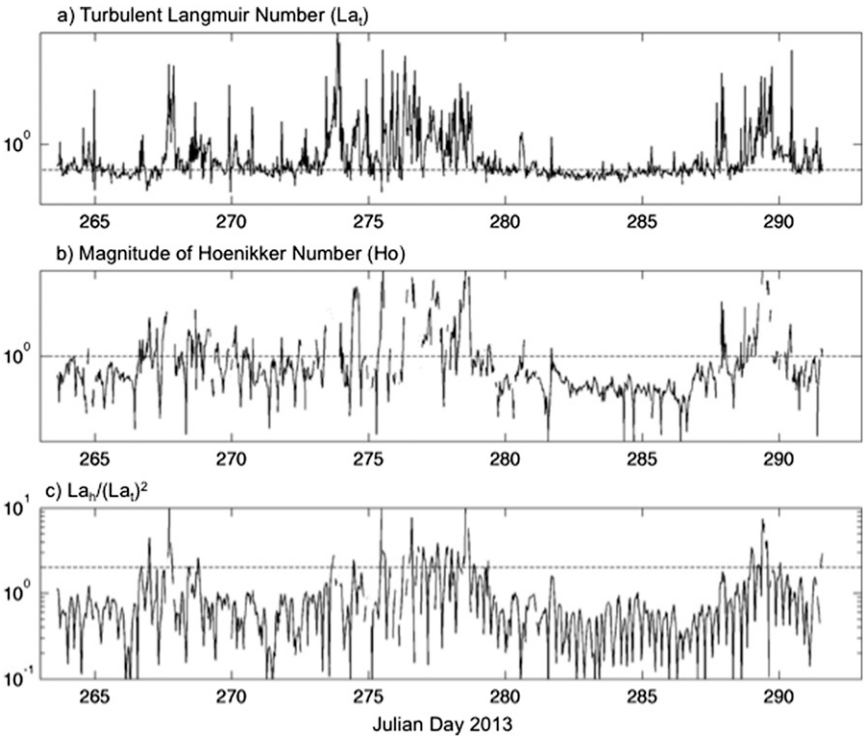

FIG. 4. Estimates of (a) the turbulent Langmuir number La_t and (b) absolute value of the Hoenikker number Ho, and (c) the ratio of bottom Langmuir number La_H to La_t vs Julian day The dashed horizontal lines corresponds to $La_t = 0.5$, Ho = 1, and $La_H/(La_t)^2 = 2$.

Langmuir forcing over convection (Fig. 4b). However, there are also periods when Ho > 1 and $La_t > 1$, suggesting dominance of the surface heat flux. Conditions where $La_H > 2La_t^2$ are rare and generally occur under weak wind and wave forcing (Fig. 4c).

b. *Example of Langmuir circulation (ADCP)*

Despite the fact that the beam spread of an ADCP results in significant horizontal averaging, the bottom-mounted ADCP provided several examples of circulation that is generally consistent with LC. To remove any high-frequency noise and low-frequency tidal motions, the ADCP data were bandpass filtered to remove motions with periods longer than 1800 s and shorter than 90 s. An example of the bandpassed velocity structure is shown in Fig. 5. These data were collected on JD 282 during the prolonged nor'easter event, during one of the few periods when the water column was fully mixed and $H_m = H$. The wind was blowing about 10 m s^{-1} from the northeast and the bandpassed velocity data in Fig. 5 have been rotated into a frame of reference aligned with the inferred orientation of LC. The velocity structure recorded by the ADCP is largely consistent with that expected due to LC. During this period, coherent and energetic vertical motions (>0.02 m s^{-1}) that extend throughout the water column pass the ADCP location approximately every 5 min. The along-cell velocity perturbation is generally positive in the downwelling regions and negative in the upwelling regions. At the surface, the across-cell velocity structure exhibits regions of divergence and convergence consistent with the observed upwelling and downwelling. There are times when the across-cell velocity exhibits vertical shear consistent with the closed cell counterrotating vortices typically associated with LC. However, most of the time, the across-cell velocity is uniform in the vertical and not consistent with the closed circulation of a vortex. The lack of a close circulation is consistent with the observations of Gargett and Wells (2007), who suggest that the circulation must be closed in the near-surface and near-bottom regions that are not resolved by an ADCP.

During this example, the bandpassed acoustic backscatter of the ADCP is elevated under regions of downwelling near the surface. We interpret this high relative backscatter near the surface as the downward advection of air bubbles generated by wave breaking at the surface (Melville 1996). Near the seabed, elevated backscatter is often associated with upwelling velocities. During this time period, the waves are energetic, with orbital velocities > 0.05 m s^{-1} at the bottom in 14 m of

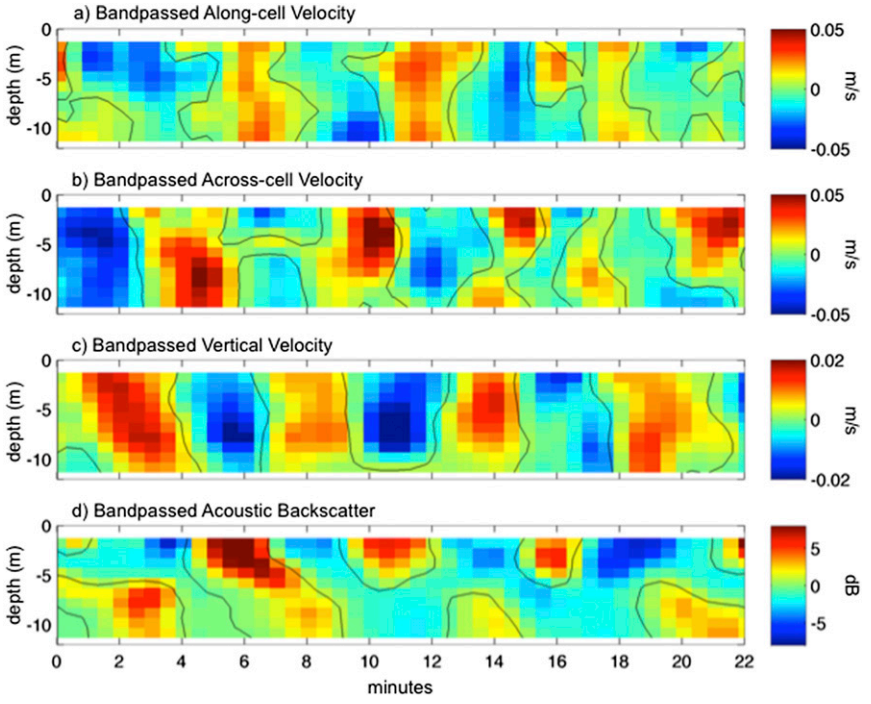

FIG. 5. Contours of bandpass [(1/1800)−(1/90) Hz] filtered velocity rotated into a coordinate system of inferred LC orientation vs depth (m): (a) along-cell velocity ($\mathrm{m\,s^{-1}}$), (b) across-cell velocity ($\mathrm{m\,s^{-1}}$), (c) vertical velocity ($\mathrm{m\,s^{-1}}$), and (d) acoustic backscatter (dB) from a bottom-mounted 1200-kHz ADCP deployed immediately adjacent to the turbulence tower. Data were collected on Julian day 282 at approximately 1500 UTC.

water. Thus, we suggest that either wave energy or tidal currents or both are of sufficient strength to resuspend the fine sediment typically found in the bay and that the upwelling velocities advect this sediment upward, elevating the relative backscatter. The observed patterns of acoustic backscatter are consistent with the observations of Langmuir supercells documented on the New Jersey continental shelf (Gargett and Wells 2007). As we will discuss below, this example comes from one of the relatively few periods when full LSCs are expected via Eq. (7). It should be noted that the ADCP was not intended to measure Langmuir circulation and with the ADCP beams oriented 20° from the vertical, the velocity measurements near the surface represent an average over horizontal spatial scales of 8–9 m. The horizontal averaging scales are smaller close to the bottom, but the large footprint of the ADCP does not adequately resolve many of the finer details of the circulation. Because of these limitations, the majority of the quantitative analysis is done with higher-quality ADV data.

c. *Characterization of Langmuir circulation (ADV data)*

The ADV data on the tower provide much higher-quality measurements of velocity than the ADCP data, albeit with coarser vertical resolution. Throughout the experiment, significant wind and wave events were associated with elevated σ_w. The highest values of σ_w were observed during the prolonged nor'easter event and are strongly correlated to significant wave height throughout the record (Fig. 6a). When normalized by u_*^2, the observed values of σ_w^2 exceed comparable measurements made near a fixed boundary (Hinze 1975) (Fig. 7). The magnitude and vertical distribution of σ_w^2/u_*^2 generally are consistent with the LES results of Sullivan et al. (2007), which include both the CL vortex force and a stochastic model for wave breaking. Their simulations with and without wave breaking are very similar, suggesting that the enhanced vertical TKE is primarily the result of LC and not wave breaking. In the simulations of Sullivan et al. (2007), $\mathrm{La}_t \sim 0.3$, which is generally consistent with the values reported here. Their results were sensitive to wave age, with greater σ_w^2/u_*^2 for fully developed waves as compared to fetch-limited conditions. The waves in Chesapeake Bay are fetch-limited, consistent with observed values of σ_w^2/u_*^2 that are smaller than the LES results of Sullivan et al. (2007).

Our estimates of σ_w^2/u_*^2 at the uppermost sensor are larger than other field observations from the open-ocean

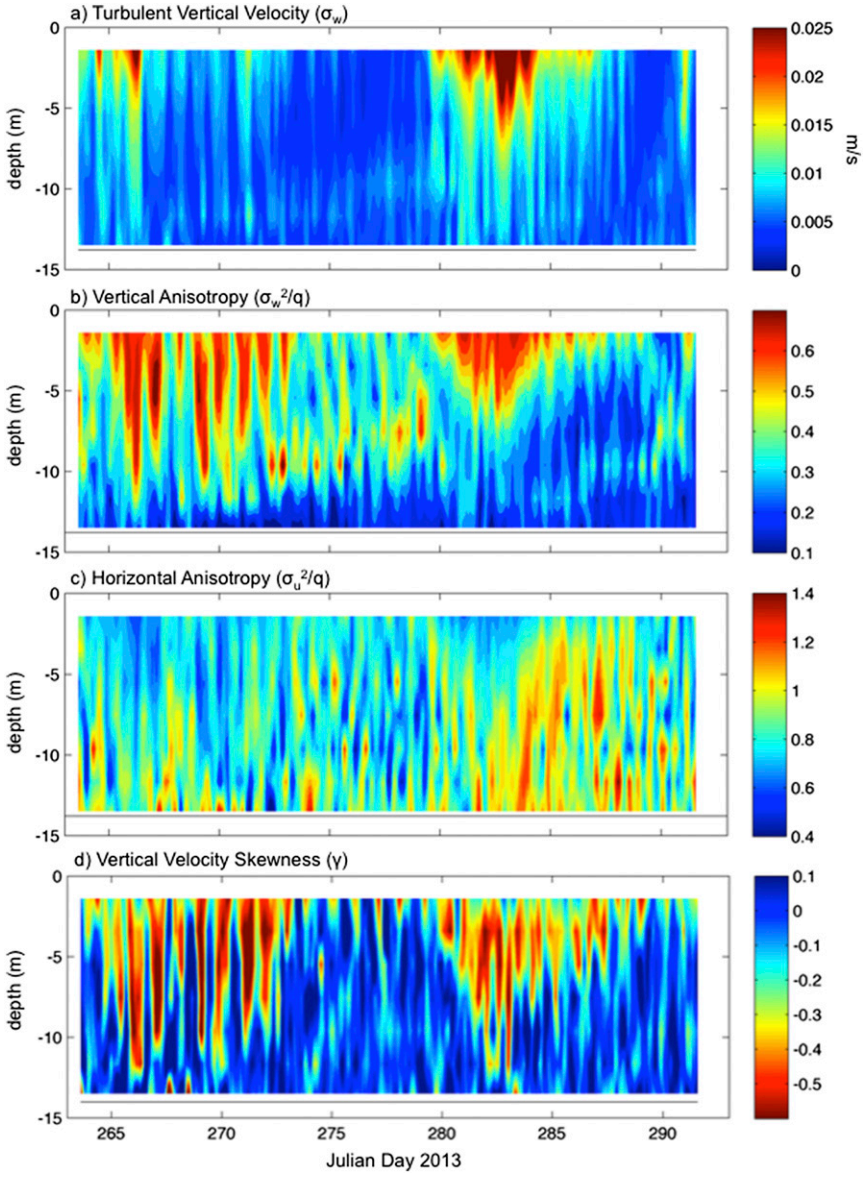

FIG. 6. Contours of (a) the turbulent vertical velocity (σ_w, m s^{-1}), (b) vertical anisotropy (σ_w^2/q), (c) horizontal anisotropy (σ_u^2/q), and (d) low-frequency (<1/20 Hz) vertical velocity skewness γ calculated from the six ADVs on the tower and the ADV on adjacent bottom lander vs Julian day. Data were smoothed with a 7-h running median for visualization.

surface mixed layer (D'Asaro 2001; Tseng and D'Asaro 2004). Additionally, we do not observe a clear subsurface maximum in σ_w^2/u_*^2 but find the highest values for the measurements made closest to the surface ($z/H_m \sim -0.1$). One potential explanation for the differences between our measurements and previously published values could simply reflect differences in measurement techniques. The Lagrangian floats used by D'Asaro (2001) and Tseng and D'Asaro (2004) do not respond to motions less than 1 m. If the turbulent motions are constrained by the distance from the boundary, the Lagrangian floats may undersample the variance in the region closest to the sea surface, where more variance may occur at smaller scales.

Periods where $La_t < 0.5$ generally correspond to conditions of increased σ_w^2/q and decreased σ_u^2/q near the surface (Figs. 6b,c). Under strong wave and wind forcing, values of σ_w^2/q approach or exceed the isotropic value ($\sigma_w^2/q \sim 2/3$). In contrast to flow adjacent to a rigid boundary, where σ_w^2/q is expected to increase with distance from the boundary (Pope 2000), the vertical anisotropy decreases with distance from the surface. For boundary layer flows, the vertical shear near the boundary

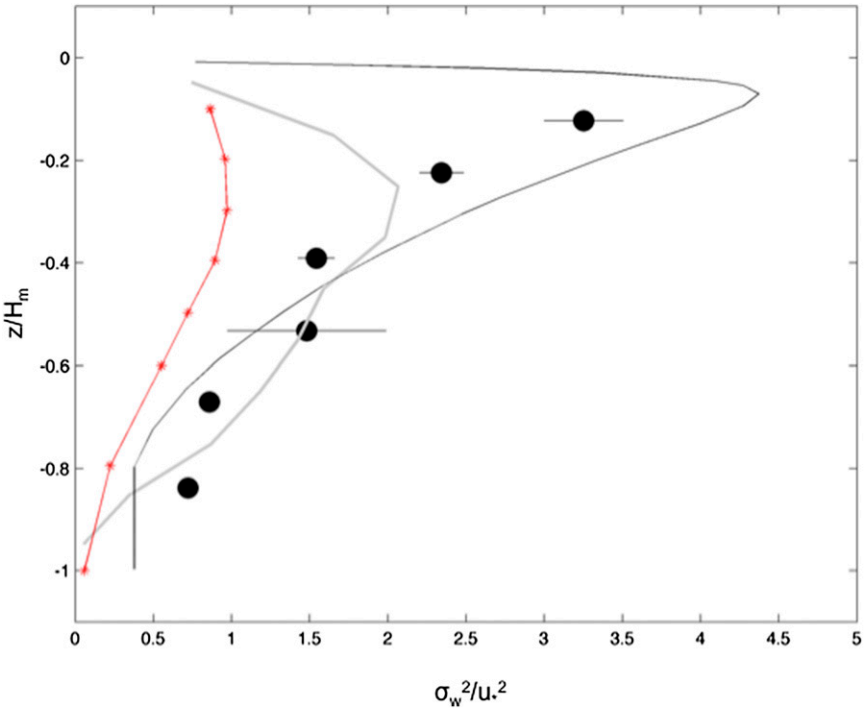

FIG. 7. Bin-averaged values of the normalized vertical velocity variance (σ_w^2/u_*^2) as a function of nondimensional depth (z/H_m). Only data with strong Langmuir forcing ($La_t < 0.5$) are included. Horizontal lines represent the 95% confidence interval, assuming a normal distribution. Solid black line is the LES results of Sullivan et al. (2007), including both Stokes drift and wave breaking (their Fig. 9), solid gray lines are the observations of Tseng and D'Asaro (2004, their Fig. 4), and the asterisks (red line) are the rough wall rigid boundary layer laboratory measurements of Hinze (1975).

is a source of anisotropy. Under conditions when LC is inferred, the observed vertical shear near the surface is much smaller than expected based on boundary layer scaling (e.g., $u_*/\kappa z$). We contend that the lack of mean shear results in turbulence that is much more isotropic than for flow adjacent to a rigid boundary. Deeper in the water column both the presence of the bottom and near-bed stratification enhance the mean vertical shear and suppress vertical turbulent motions contributing to the increase in anisotropy (decreased σ_w^2/q and increased σ_u^2/q).

While there are significant differences in anisotropy in the upper portion of the water column when $La_t < 0.5$, significant differences are not observed near the bed. In fact, the anisotropy at the bottom ADV for conditions where $La_t < 0.5$ is not statistically different from

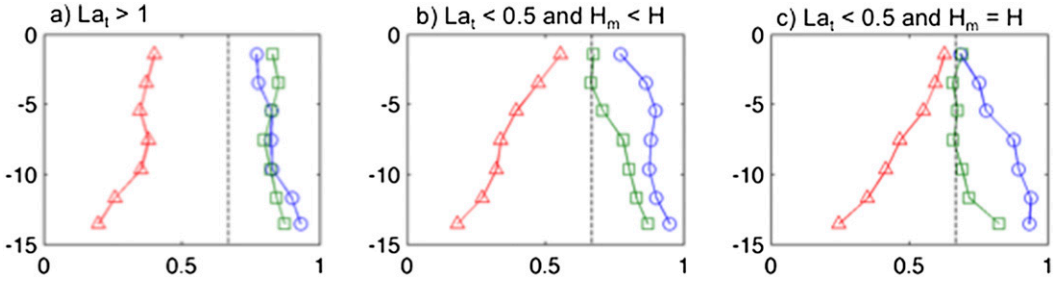

FIG. 8. Profiles of σ_u^2/q (blue circles), σ_v^2/q (green squares), and σ_w^2/q (red triangles) for conditions when (a) Langmuir circulation is not expected (e.g., $La_t > 1$); (b) Langmuir circulation is expected but depth-limited by stratification (e.g., $La_t < 0.5$ and $H_m < H$); and (c) Langmuir circulation is expected, and full water column Langmuir circulation is possible (e.g., $La_t < 0.5$ and $H_m = H$). In each panel, vertical dashed line represents isotropic conditions (e.g., $\sigma_u^2 = \sigma_v^2 = \sigma_w^2$).

conditions where $La_t > 1$ (Fig. 8). Further, while there are brief periods of weak stratification when full water column LSCs are observed (e.g., Fig. 5), we see no clear evidence for an intensified downwind jet and enhanced near-bed σ_u^2/q. Conditions where $La_t < 0.5$ and $H_m = H$ have values of σ_u^2/q near the bed that are not statistically different at the 95% confidence interval from conditions where $La_t < 0.5$ and stratification limits H_m to less than the full water depth. Near the surface, conditions when full water column LSCs are inferred have slightly larger values of σ_w^2/q and smaller values of σ_u^2/q than conditions where stratification is inferred to limit the depth of LC, but these differences are modest.

Consistent with the spatial and temporal patterns of σ_w^2 and σ_w^2/q, periods with significant wind and wave forcing generally have $\gamma < -0.4$ (Fig. 6d). However, unlike σ_w^2, which is greatest at the ADV $\sim$ 1.5 m from the surface, values of γ are generally more negative at the ADV $\sim$ 3.5 m from the surface. Events with negative skewness often penetrate to a depth greater than 10 m, sometimes extending throughout the water column. Periods of low wind forcing and/or internal wave activity are generally characterized by positive vertical velocity skewness (e.g., JD 274–280). Near the seabed, where shear-driven bottom boundary layer turbulence is expected to dominate, mean values of γ are $\sim$0 with no clear variability associated with wind or wave forcing.

Negative values of γ are indicative of strong short-lived downwelling events alternating with weaker longer-lived upwelling events. Negative vertical velocity skewness has been used to indicate both the presence of LC (Sullivan et al. 2007) and unstable convection (Moeng and Rotunno 1990). As we discuss in more detail in section 4, strong wind and wave forcing at this location often results in conditions that are favorable for both LC and convection and distinguishing between these two processes is difficult. However, the period of JD 267 to 271 provides a clear example of conditions when the surface heat flux modulates the surface mixed layer dynamics. During this period, both wind speed and significant wave height are generally increasing, with mean values of 5 m s^{-1} and 0.36 m, respectively. During this period $0.5 < La_t < 1$, with a median value of 0.6. Both σ_w and γ show clear diurnal variability, with maximum values of σ_w and minimum values of γ generally occurring during the early morning hours following periods of outward heat flux ($Q < 0$) (Fig. 9). The periods with higher values of σ_w and negative values of γ typically have values of $Ho > 1$, suggesting that destabilizing convection is controlling the diurnal variability that is observed. Alternatively, the diurnal variations seen in Fig. 9 could be the result of LC, which is shut down by stratification associated with diurnal surface heating ($Q > 0$). When Q is positive during this period, there is a significant reduction in σ_w and γ is often positive throughout much of the water. During this period, thermal stratification near the surface develops each day associated with surface heating (Fig. 9b), which could be sufficient to suppress LC. The relative role of LC and convection will be examined further in section 4.

The spatial and temporal distribution of $r_{\min}$ generally agrees with γ (Fig. 10a). The most negative correlations generally occur during elevated waves events when $La_t < 0.5$. Consistent with the observed distribution of γ, the minimum correlation is most negative at the second ADV from the surface during strong wave forcing (e.g., JD 283). There is a secondary region of elevated correlation near the bed that is associated with internal wave motions on the pycnocline, but these motions do not exhibit negative γ and generally have less vertical velocity variance. The inferred orientation of the circulation θ_{cell} agrees reasonably well with the observed wind and wave directions (Fig. 10b), consistent with a circulation that has a positive velocity perturbation in the downwind direction that is associated with downwelling regions. However, the inferred LC orientation is consistently 45° to the left of the wind, and the LC orientation is more consistent with the mean wave direction. This is inconsistent with previous observations that have noted LC orientation to the right of the wind (e.g., Faller 1964). Our observations demonstrate that the wind and wave directions are not always aligned and that the wave direction has a tendency to be more aligned with the along-estuary axis of the channel than the wind forcing. We speculate that the waves align more with the dominant axis of fetch, which in a narrow system like Chesapeake Bay does not always align with the wind. Van Roekel et al. (2012) found that LC orientation was generally somewhere between the wind direction and wave direction when the two forces were not aligned. We infer circulations that are more aligned with the waves.

d. Modulation by stratification and tides

Unlike many open-ocean environments, Chesapeake Bay has persistent salinity stratification associated with the riverine input of buoyant freshwater. Horizontal density gradients lead to rapid restratification after mixing events, and the water column is seldom completely well mixed. Our measurement site is located on the broad western shoal adjacent to the main channel ($\sim$30 m), and even when conditions are well mixed at the tower, there is always stratification over the channel (data not shown). To assess the importance of stratification

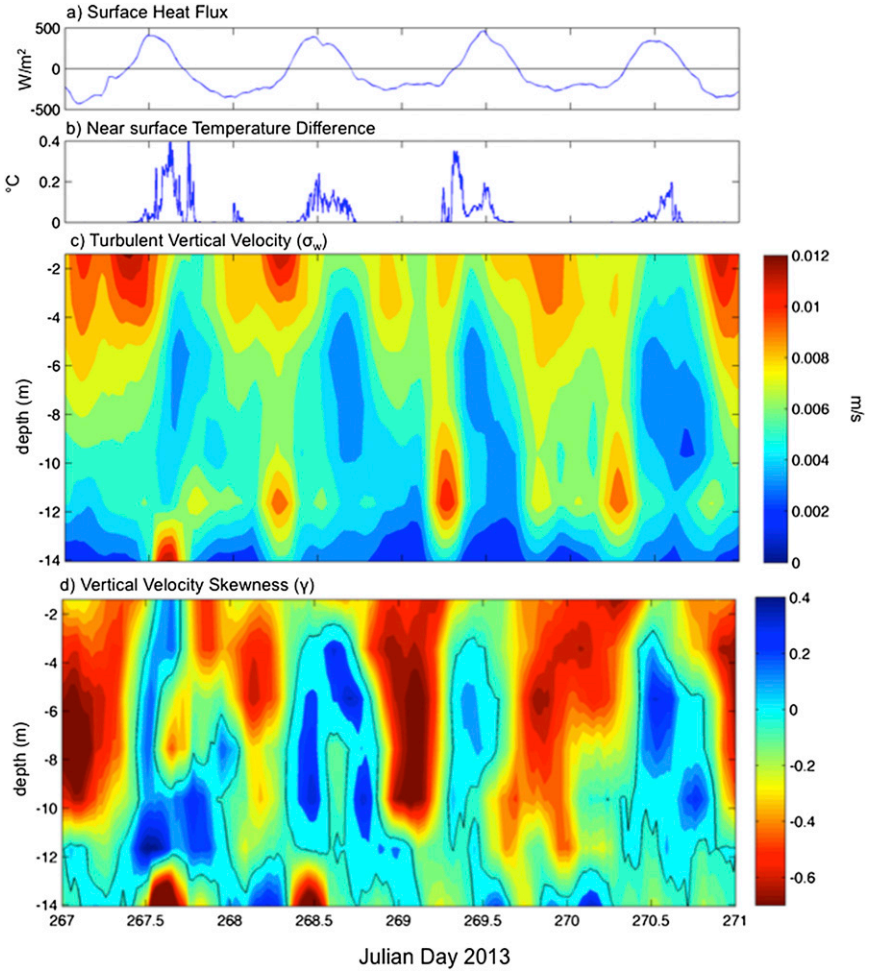

FIG. 9. Detailed conditions for Julian day 267–271 including (a) surface heat flux ($\mathrm{W\,m^{-2}}$); (b) near-surface temperature difference (°C) between the thermistors at $z \sim 1.3$ and $z \sim 2.2$ m; (c) contours of turbulent vertical velocity σ_w ($\mathrm{m\,s^{-1}}$) from the six tower ADVs and the bottom-mounted ADV on the adjacent bottom lander; and (d) contours of low-frequency vertical velocity skewness γ from the six tower ADVs and the bottom-mounted ADV on the adjacent bottom lander

on our observations of LC, we use the criteria of Li and Garrett (1997) to estimate H_m [Eq. (7)]. Our estimates of H_m are less than the full water depth for 95% of the data, and we conclude that the observed salinity stratification is almost always strong enough to prevent full water column LSCs during this experiment. The persistent salinity stratification not only prevents full water column LSCs, but also limits the vertical extent of the bottom boundary layer. We estimate the height of the bottom boundary layer by simply finding the deepest location where the gradient Richardson number Ri_g exceeds 1, based on the mean vertical shear and density stratification measured between adjacent sensors on the tower. Figure 11 compares the location of the bottom boundary layer with our estimate H_m from Eq. (7). Under strong wind and wave forcing there are conditions where the surface and bottom boundary layers overlap. However, for the majority of the experiment, the stratification is sufficient to isolate the bottom boundary layer from the surface boundary layer.

The scaling of Gargett and Grosch (2014) suggests bottom turbulence impacts LC when $\mathrm{La}_H > 2\mathrm{La}_t^2$. While this criterion is satisfied for roughly 10% of our data, we propose that in order for bottom-generated turbulence to influence LC, the surface and bottom boundary layers must overlap. During this experiment nearly all of the data where $\mathrm{La}_H > 2\mathrm{La}_t$ occur under conditions of weak wind and wave forcing, when we infer that the surface and bottom boundary layers do not overlap (e.g.,

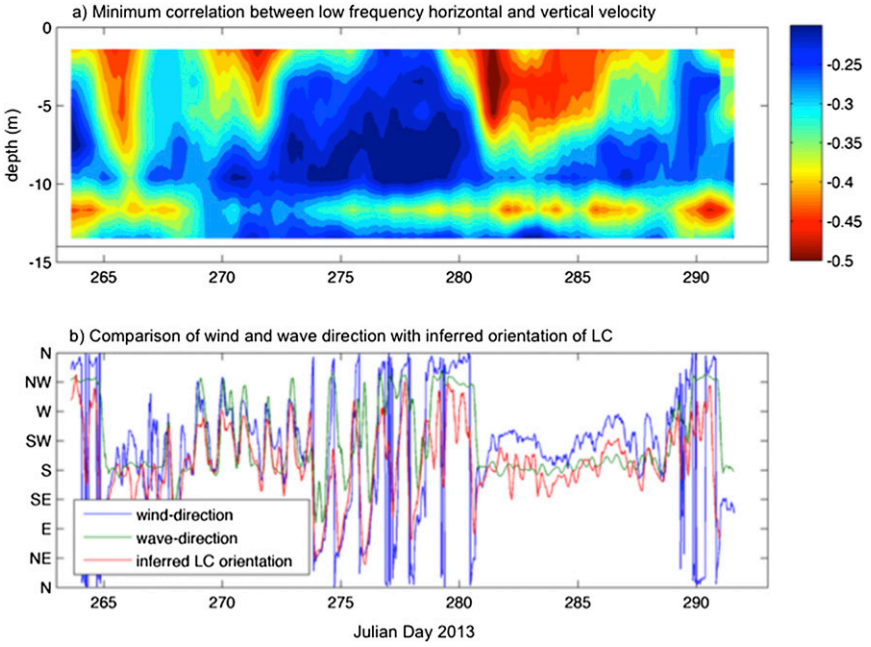

FIG. 10. (a) Contours of the minimum correlation between the low-frequency (<1/20 Hz) vertical and horizontal velocity from the six ADVs on the tower and adjacent ADV on bottom lander. Data were rotated to find the minimum (i.e., most negative) correlation between horizontal and vertical velocity. The data have been smoothed with a 35-h running median filter. (b) Comparison of the observed wind direction (blue), wave direction (green), and the direction obtained by rotating the horizontal velocity (red) to minimize its correlation with vertical velocity (from upper ADV), which we interpret as the orientation of the LC.

Fig. 11). These data generally correspond to conditions when $La_t > 1$, when circulation consistent with LC is not observed. Less than 1% of the data correspond to conditions where $La_H > 2La_t$ and $La_t < 0.5$. During the nor'easter event, our estimates suggest that the surface and bottom boundary layers overlap. However, during this period, we see no clear tidal modulation of either the intensity (σ_w^2/u_*^2) or the inferred coherence (γ or $r_{\min}$) of the observed circulations, suggesting that tidal processes play a relatively minor role in modulating LC in this environment.

While there is no clear tidal modulation in our observations, it is certainly possible that water column shear could distort coherent circulations. Following the scaling of Kukulka et al. (2011), we compare the advective time scale associated with LC (T_{LC}) to the across-wave shear time scale ($T_{du/dz}$). Assuming an aspect ratio of ~1, the advective time scale for LC can be estimated simply as H_m/σ_w. We calculate the shear time scale simply as the inverse of the magnitude of the depth-averaged across-wave shear. For conditions where the advective time scale is considerably longer than the shear time scale, we would expect significant distortion of the observed circulation. A histogram of ratio $T_{\mathrm{LC}}/T_{du/dz}$ (Fig. 12) shows that T_{LC} is never shorter than $T_{du/dz}$, with a median ratio of $T_{\mathrm{LC}}/T_{du/dz} \sim 50$. Thus, we expect that any coherent circulations in Chesapeake Bay are going to be significantly distorted by the across-wind/wave tidal shear.

4. Discussion and conclusions

The data presented above are consistent with previous observations and LES of LC. However, many of the characteristics we document also are consistent with convection. Strong wind forcing typically results in increased wave energy and Stokes drift as well as surface heat loss. As a result, wind forcing leads to conditions that are conducive to LC and convection. Given the tight coupling between the forcings, separating the contributions from shear-driven mixing, Langmuir turbulence, and convection is challenging. We take a very simplistic approach here and assume that convection dominates when $\mathrm{Ho} > 1$, shear-driven turbulence dominates when $\mathrm{Ho} < 1$, and $La_t > 1$ and LC dominates when $\mathrm{Ho} < 1$ and $La_t < 1$. This simple approach suggests that surface shear–driven turbulence is the dominant mixing mechanism for only ~9% of this experiment, consistent with the results of Gargett and Grosch (2014). Convection is the dominant source of turbulence in the surface

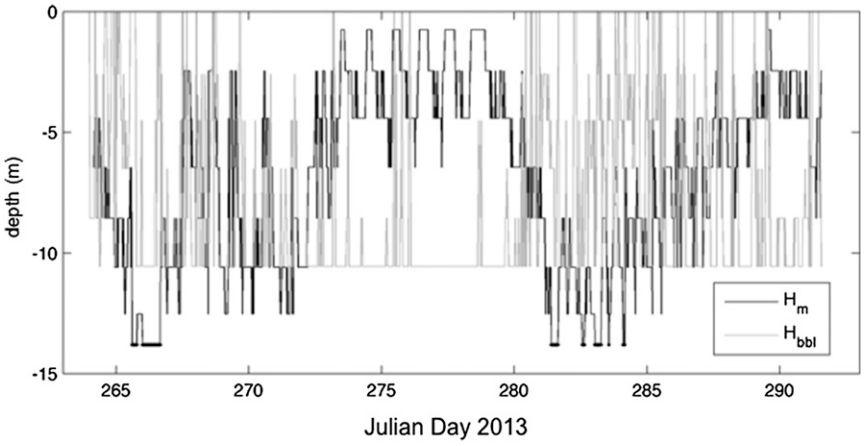

FIG. 11. The inferred vertical location of the depth of the surface mixed layer H_m (black line) and the top of the bottom boundary layer H_{bbl} (gray line). The H_m is estimated from Eq. (7), and H_{bbl} is estimated from the location nearest the bed where the $\mathrm{Ri}_g > 1$. Merged black dots at $z = -13.8$ m represent conditions when full water column Langmuir circulation is predicted (e.g., $H_m = H$).

boundary layer ~15% of the time, with the remaining 76% of the conditions dominated by Langmuir turbulence. In a fetch-limited environment like Chesapeake Bay, there is a strong relationship between u_* and U_S, and $u_{*_{\mathrm{LC}}}$ is nearly always greater than u_* when there is significant wind forcing resulting in $\mathrm{La}_t < 1$.

Given the absence of surface shear–driven turbulence, we revisit the vertical profiles of σ_w^2 presented in section 3c. The same data are presented in Fig. 13, but we distinguish between conditions where LC is expected to dominate (e.g., Ho < 1 and $\mathrm{La}_t < 0.5$) and times that convective mixing is inferred to be the primary source of energy (e.g., Ho > 1). Conditions where $\mathrm{La}_t < 0.5$ can have either a stabilizing or destabilizing surface heat flux, so we further segregate the data based on the sign of Q. For the three cases considered, near-surface values of σ_w^2/u_*^2 are elevated relative to previous results collected adjacent to a rigid boundary. Further, we see no statistically significant differences between stabilizing and destabilizing heat fluxes (Fig. 13) when Langmuir turbulence is expected to dominate. For these conditions, values of σ_w^2 normalized by $u_{*_{\mathrm{LC}}}^2$ agree favorably with the rigid boundary layer data of Hinze (1975), suggesting that this is the appropriate velocity scale for Langmuir turbulence. Under conditions when we expect significant convection (Ho > 1), near-surface values of σ_w^2/u_*^2 also are elevated, and the elevated values of σ_w^2/u_*^2 extend deeper into the surface mixed layer (Fig. 13). Normalizing these data by w_*^2 effectively collapses the data so that they are consistent both with our data where $u_{*_{\mathrm{LC}}} > w_*$ and with the rigid boundary layer results of Hinze (1975).

Next, we compare vertical profiles of γ and $r_{\min}$ based on the inferred source of turbulent energy (Fig. 14). There are differences in γ for conditions when we expect LC to dominate based on the sign of the surface heat flux. Destabilizing heat flux appears to slightly enhance the negative vertical velocity skewness, particularly in the lower portion of the water column ($z/H_m < -0.4$). Values of γ are even more negative for conditions where $w_* > u_{*_{\mathrm{LC}}}$, suggesting that convection contributes significantly to the observed negative vertical velocity skewness. In contrast to values of γ, values of $r_{\min}$ are more negative for conditions where we infer mixing driven primarily by LC (Fig. 14b). We do not see statistically significant differences in $r_{\min}$ because of the

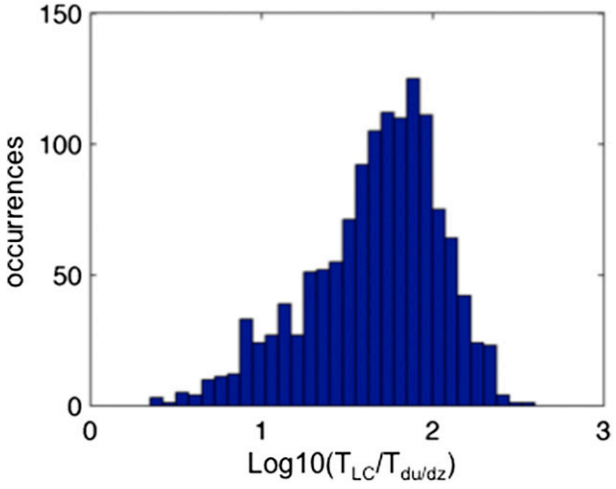

FIG. 12. Histogram of the $\log_{10}$ value of the ratio of the advective time scale associated with Langmuir circulation T_{LC} to advective time scale associated with vertical shear $T_{du/dz}$. Median value is ~50 with no values of $T_{\mathrm{LC}} < T_{du/dz}$ indicating significant distortion by tidal shear.

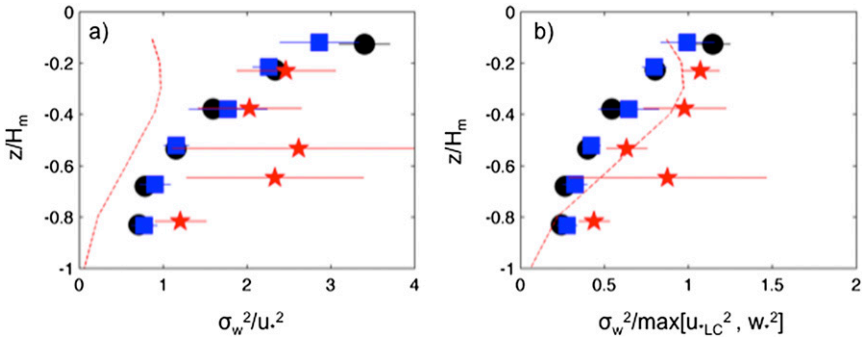

FIG. 13. Bin-averaged values of the normalized vertical velocity variance as a function of nondimensional depth (z/H_m) for conditions where Langmuir forcing dominates but with unstable convection (black circles = $La_t < 0.5$, $0 < Ho < 1$); conditions where Langmuir circulation is expected, but surface heat flux is stabilizing (blue squares = $La_t < 0.5$, $Ho < 0$); and conditions where convection is expected to dominate (red stars = $Ho > 1$). Horizontal lines represent 95% confidence interval assuming the data are normally distributed, and the dashed line is the rough wall rigid boundary layer laboratory measurements of Hinze (1975). In (a), data are nondimensionalized by u_* and in (b) the data are nondimensionalized by either $u_{*_{LC}}$ or w_* depending on which is larger.

sign of the surface heat flux for conditions when $u_{*_{LC}} > w_*$. However, throughout most of the surface mixed layer, the correlation is more negative when LC is inferred as the dominant source of turbulence than for convection. It is important to note that conditions where $w_* > u_{*LC}$ typically also have significant LC forcing. In an attempt to further isolate these two processes, we plot the values of γ and r_{min} as a function of $u_{*_{LC}} > w_*$ (Fig. 15) for conditions where $La_t < 0.5$ and $w_* > 0$. While the data are noisy, increased values of $u_{*_{LC}} > w_*$ generally correspond to 1) decreased vertical velocity skewness (i.e., increased γ) and 2) increased low-frequency (<1/20 Hz) correlation (i.e., negative r_{min}). Our interpretation of these data are that the enhanced vertical velocity skewness is driven primarily by convection, while the increased coherence is more a function of circulation consistent LC. It should be noted that while some LES results suggest LC causes negative vertical velocity skewness (McWilliams et al. 1997; Sullivan et al. 2007), others show nearly symmetric upwelling and downwelling flows (Tejada-Martinez and Grosch 2007).

As demonstrated in section 3c, the inferred cell orientation (θ_{cell}) agrees favorably with the observed wave direction. This is consistent with forcing by the CL vortex force. In the absence of other forcing, we would not expect convection to result in a similar agreement between θ_{cell} and Θ. Figure 16 compares the difference between the inferred cell orientation and the dominant wave direction (e.g., $\theta_{cell} - \Theta$) for conditions where $Ho > 1$ with conditions where $Ho < 1$ and $La_t < 0.5$. Strong LC forcing corresponds to a narrow distribution of $\theta_{cell} - \Theta$ with a median value of $-13°$, suggesting cells that are roughly aligned with the direction of wave propagation with low variability. In contrast, under destabilizing heat flux and weak LC forcing, the median

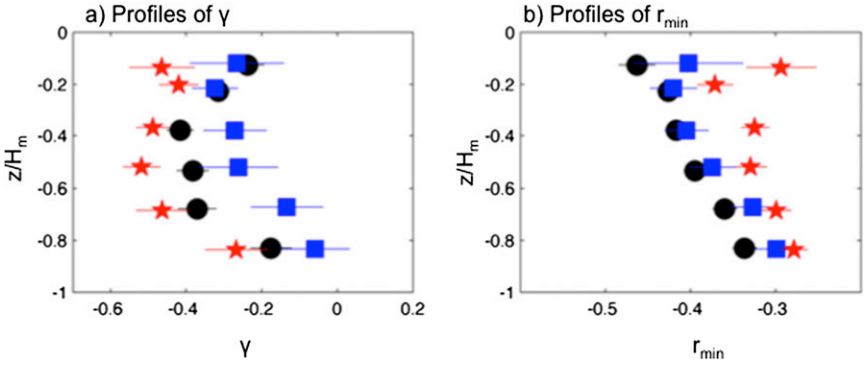

FIG. 14. As in Fig. 13, but for (a) γ and (b) r_{min} as a function of nondimensional depth z/H_m.

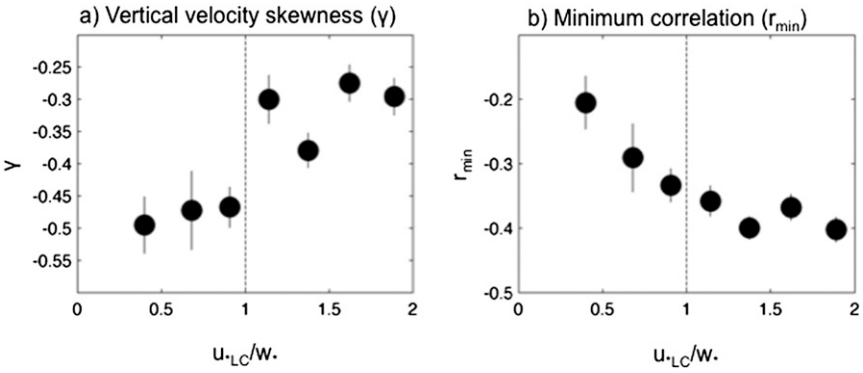

FIG. 15. Bin-averaged values of (a) γ and (b) $r_{\min}$ as a function of the ratio $u_{*_{Lc}}/w_*$ for conditions when $La_t < 0.5$ and $Ho > 0$ (destabilizing heat loss). All data from within the surface mixed layer ($z/H_m < 1$) are included. Vertical lines on the black circles represent 95% confidence interval, assuming the data are normally distributed, and the dashed vertical line presents the proposed threshold between Langmuir and convective forcing.

value of $\theta_{\text{cell}} - \Theta$ is $-39°$. More importantly under strong convective forcing, the distribution is broad suggesting no preferred orientation of the observed circulation cell.

We conclude that under moderate to strong wind forcing, circulations consistent with LC are the dominant mechanism that results in mixing in the surface boundary layer of Chesapeake Bay. Under these conditions, the surface waves that are the source of the CL vortex force usually are breaking. Scully and Trowbridge (2015, manuscript submitted to *J. Phys. Oceanogr.*) provide evidence that wave breaking at this location dominates the surface energetics and momentum flux at this location. While wave breaking and LC are often thought of as separate processes, there is growing evidence that they are coupled (e.g., Sullivan et al. 2007). Breaking waves generate vertical vorticity, which interact with the wave-induced Stokes drift shear to create streamwise vorticity. Consistent with the data presented above, this process results in downwelling that corresponds to intensified flow in the direction of wave propagation centered under the region of breaking. As described by Sullivan et al. (2007) and consistent with the model suggested by Csanady (1994) and Teixeira and Belcher (2002), wave breaking can provide the necessary "seed" vorticity to initiate the CL instability. We hypothesize that this conceptual model of coherent circulations driven by the interaction of wave breaking and the Stokes drift shear is the dominant turbulent process in the surface boundary layer of Chesapeake Bay. The absence of direct surface-stress-driven mixing in our data is consistent with recent work in other coastal environments (Gargett and Grosch 2014) and provides additional evidence that mixing in the surface boundary layer of the ocean is fundamentally driven by the presence of waves.

Acknowledgments. We thank two anonymous reviewers for their comments on this manuscript. The funding

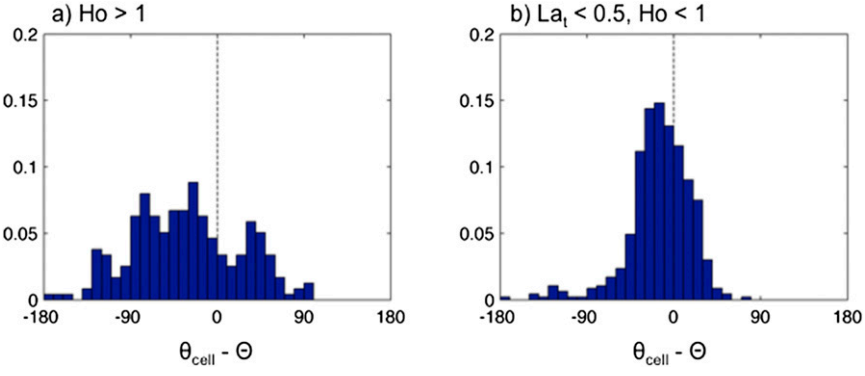

FIG. 16. Histograms of the difference between the inferred cell orientation θ_{cell} and the dominant wave direction Θ for conditions when (a) convection is expected to dominate ($Ho > 1$) and (b) Langmuir turbulence is expected to dominate ($La_t < 0.5$, $Ho < 1$).

for this research was provided by the National Science Foundation Grants OCE-1339032 and OCE-1338518.

REFERENCES

Belcher, S. E., A. L. Grant, K. E. Hanley, B. Fox-Kemper, L. Van Roekel, P. P. Sullivan, and J. A. Polton, 2012: A global perspective on Langmuir turbulence in the ocean surface boundary layer. *Geophys. Res. Lett.*, **39**, L18605, doi:10.1029/2012GL052932.

Craik, A. D. D., and S. Leibovich, 1976: A rational model for Langmuir circulations. *J. Fluid Mech.*, **73**, 401–426, doi:10.1017/S0022112076001420.

Csanady, G. T., 1994: Vortex pair model of Langmuir circulation. *J. Mar. Res.*, **52**, 559–581, doi:10.1357/0022240943076984.

D'Asaro, E. A., 2001: Turbulent vertical kinetic energy in the ocean mixed layer. *J. Phys. Oceanogr.*, **31**, 3530–3537, doi:10.1175/1520-0485(2002)031<3530:TVKEIT>2.0.CO;2.

Fairall, C. W., E. F. Bradley, D. P. Rogers, J. B. Edson, and G. S. Young, 1996: Bulk parameterization of air-sea fluxes for Tropical Ocean-Global Atmosphere Coupled-Ocean Atmosphere Response Experiment. *J. Geophys. Res.*, **101**, 3747–3764, doi:10.1029/95JC03205.

Faller, A. J., 1964: The angle of windrows in the ocean. *Tellus*, **16A**, 363–370, doi:10.1111/j.2153-3490.1964.tb00173.x.

Fisher, A., L. Sanford, and S. Suttles, 2015: Wind stress dynamics in Chesapeake Bay: Spatiotemporal variability and wave dependence in a fetch-limited environment. *J. Phys. Oceanogr.*, **45**, 2679–2696, doi:10.1175/JPO-D-15-0004.1.

Gargett, A. E., and J. R. Wells, 2007: Langmuir turbulence in shallow water. Part 1. Observations. *J. Fluid Mech.*, **576**, 27–61, doi:10.1017/S0022112006004575.

——, and C. E. Grosch, 2014: Turbulence processes domination under the combined forcings of wind stress, the Langmuir vortex force, and surface cooling. *J. Phys. Oceanogr.*, **44**, 44–67, doi:10.1175/JPO-D-13-021.1.

——, J. Wells, A. E. Tejada-Martinez, and C. E. Grosch, 2004: Langmuir supercells: A mechanism for sediment resuspension and transport in shallow seas. *Science*, **306**, 1925–1928, doi:10.1126/science.1100849.

Gerbi, G. P., J. H. Trowbridge, E. A. Terray, A. J. Plueddemann, and T. Kukulka, 2009: Observations of turbulence in the ocean surface boundary layer: Energetics and transport. *J. Phys. Oceanogr.*, **39**, 1077–1096, doi:10.1175/2008JPO4044.1.

Grant, A. L., and S. E. Belcher, 2009: Characteristics of Langmuir turbulence in the ocean mixed layer. *J. Phys. Oceanogr.*, **39**, 1871–1887, doi:10.1175/2009JPO4119.1.

Harcourt, R. R., and E. A. D'Asaro, 2008: Large-eddy simulation of Langmuir turbulence in pure wind seas. *J. Phys. Oceanogr.*, **38**, 1542–1562, doi:10.1175/2007JPO3842.1.

Hinze, J. O., 1975: *Turbulence*. 2nd ed. Mc-Graw Hill, 790 pp.

Johnson, D., 2002: DIWASP: Directional Wave Spectra Toolbox, version 1.1, for MATLAB: User manual. Centre for Water Research, University of Western Australia Research Rep. WP 1601 DJ (V1.1), 18 pp.

Jones, N. L., and S. G. Monismith, 2007: Measuring short-period wind waves in a tidally forced environment with a subsurface pressure gauge. *Limnol. Oceanogr. Methods*, **5**, 317–327, doi:10.4319/lom.2007.5.317.

Kaimal, J. C., J. C. Wyngaard, Y. Izumi, and O. R. Cote, 1972: Spectral characteristics of surface-layer turbulence. *Quart. J. Roy. Meteor. Soc.*, **98**, 563–589, doi:10.1002/qj.49709841707.

Kenyon, K. E., 1969: Stokes drift for random gravity waves. *J. Geophys. Res.*, **74**, 6991–6994, doi:10.1029/JC074i028p06991.

Kitaigorodskii, S. A., 1983: On the theory of the equilibrium range in the spectrum of wind-generated gravity waves. *J. Phys. Oceanogr.*, **13**, 816–827, doi:10.1175/1520-0485(1983)013<0816:OTTOTE>2.0.CO;2.

Kukulka, T., A. J. Plueddemann, J. H. Trowbridge, and P. P. Sullivan, 2010: Rapid mixed layer deepening by the combination of Langmuir and shear instabilities: A case study. *J. Phys. Oceanogr.*, **40**, 2381–2400, doi:10.1175/2010JPO4403.1.

——, ——, ——, and ——, 2011: The influence of crosswind tidal currents on Langmuir circulation in a shallow ocean. *J. Geophys. Res.*, **116**, C08005, doi:10.1029/2011JC006971.

Leibovich, S., 1983: The form and dynamics of Langmuir circulations. *Annu. Rev. Fluid Mech.*, **15**, 391–427, doi:10.1146/annurev.fl.15.010183.002135.

——, and S. Paolucci, 1981: The instability of the ocean to Langmuir circulations. *J. Fluid Mech.*, **102**, 141–167, doi:10.1017/S0022112081002589.

Li, M., and C. Garrett, 1995: Is Langmuir circulation driven by surface waves or surface cooling? *J. Phys. Oceanogr.*, **25**, 64–76, doi:10.1175/1520-0485(1995)025<0064:ILCDBS>2.0.CO;2.

——, and ——, 1997: Mixed layer deepening due to Langmuir circulation. *J. Phys. Oceanogr.*, **27**, 121–132, doi:10.1175/1520-0485(1997)027<0121:MLDDTL>2.0.CO;2.

Lumley, J. L., and E. A. Terray, 1983: Kinematics of turbulence convected by a random wave field. *J. Phys. Oceanogr.*, **13**, 2000–2007, doi:10.1175/1520-0485(1983)013<2000:KOTCBA>2.0.CO;2.

McWilliams, J. C., P. P. Sullivan, and C. H. Moeng, 1997: Langmuir turbulence in the ocean. *J. Fluid Mech.*, **334**, 1–30, doi:10.1017/S0022112096004375.

Melville, W. K., 1996: The role of surface-wave breaking in air-sea interaction. *Annu. Rev. Fluid Mech.*, **28**, 279–321, doi:10.1146/annurev.fl.28.010196.001431.

Min, H. S., and Y. Noh, 2004: Influence of the surface heating on Langmuir circulation. *J. Phys. Oceanogr.*, **34**, 2630–2641, doi:10.1175/JPOJPO-2654.1.

Moeng, C. H., and R. Rotunno, 1990: Vertical-velocity skewness in the buoyancy-driven boundary layer. *J. Atmos. Sci.*, **47**, 1149–1162, doi:10.1175/1520-0469(1990)047<1149:VVSITB>2.0.CO;2.

Noh, Y., H. S. Min, and S. Raasch, 2004: Large eddy simulation of the ocean mixed layer: The effects of wave breaking and Langmuir circulation. *J. Phys. Oceanogr.*, **34**, 720–735, doi:10.1175/1520-0485(2004)034<0720:LESOTO>2.0.CO;2.

Pawka, S. S., 1983: Island shadows in wave directional spectra. *J. Geophys. Res.*, **88**, 2579–2591, doi:10.1029/JC088iC04p02579.

Phillips, W. R. C., 2001: On an instability to Langmuir circulations and the role of Prandtl and Richardson numbers. *J. Fluid Mech.*, **442**, 335–358, doi:10.1017/S0022112001005110.

Plueddemann, A. J., J. A. Smith, D. M. Farmer, R. A. Weller, W. R. Crawford, R. Pinkel, and A. Gnanadesikan, 1996: Structure and variability of Langmuir circulation during the Surface Waves Processes Program. *J. Geophys. Res.*, **101**, 3525–3543, doi:10.1029/95JC03282.

Polton, J. A., and S. E. Belcher, 2007: Langmuir turbulence and deeply penetrating jets in an unstratified mixed layer. *J. Geophys. Res.*, **112**, C09020, doi:10.1029/2007JC004205.

Pope, S. B., 2000: *Turbulent Flows*. Cambridge University Press, 773 pp.

Shay, T. J., and M. C. Gregg, 1986: Convectively driven turbulent mixing in the upper ocean. *J. Phys. Oceanogr.*, **16**, 1777–1798, doi:10.1175/1520-0485(1986)016<1777:CDTMIT>2.0.CO;2.

Skyllingstad, E. D., and D. W. Denbo, 1995: An ocean large-eddy simulation of Langmuir circulations and convection in the surface mixed layer. *J. Geophys. Res.*, **100**, 8501–8522, doi:10.1029/94JC03202.

Smith, J. A., 1992: Observed growth of Langmuir circulation. *J. Geophys. Res.*, **97**, 5651–5664, doi:10.1029/91JC03118.

Sullivan, P. P., J. C. McWilliams, and W. K. Melville, 2007: Surface gravity wave effects in the oceanic boundary layer: Large-eddy simulation with vortex force and stochastic breakers. *J. Fluid Mech.*, **593**, 405–452, doi:10.1017/S002211200700897X.

Teixeira, M. A. C., and S. E. Belcher, 2002: On the distortion of turbulence by a progressive surface wave. *J. Fluid Mech.*, **458**, 229–267, doi:10.1017/S0022112002007838.

Tejada-Martinez, A. E., and C. E. Grosch, 2007: Langmuir turbulence in shallow water. Part 2. Large-eddy simulation. *J. Fluid Mech.*, **576**, 63–108, doi:10.1017/S0022112006004587.

——, ——, N. Sinha, C. Akan, and G. Martinat, 2012: Disruption of the bottom log layer in large-eddy simulations of full-depth Langmuir circulation. *J. Fluid Mech.*, **699**, 79–93, doi:10.1017/jfm.2012.84.

Tseng, R. S., and E. A. D'Asaro, 2004: Measurements of turbulent vertical kinetic energy in the ocean mixed layer from Lagrangian floats. *J. Phys. Oceanogr.*, **34**, 1984–1990, doi:10.1175/1520-0485(2004)034<1984:MOTVKE>2.0.CO;2.

Van Roekel, L. P., B. Fox-Kemper, P. P. Sullivan, P. E. Hamlington, and S. R. Haney, 2012: The form and orientation of Langmuir cells for misaligned winds and waves. *J. Geophys. Res.*, **117**, C05001, doi:10.1029/2011JC007516.

Voulgaris, G., and J. H. Trowbridge, 1998: Evaluation of the acoustic Doppler velocimeter (ADV) for turbulence measurements. *J. Atmos. Oceanic Technol.*, **15**, 272–289, doi:10.1175/1520-0426(1998)015<0272:EOTADV>2.0.CO;2.

Weller, R. A., and J. F. Price, 1988: Langmuir circulation within the oceanic mixed layer. *Deep-Sea Res.*, **35A**, 711–747, doi:10.1016/0198-0149(88)90027-1.

——, J. P. Dean, J. F. Price, E. A. Francis, J. Marra, and D. C. Boardman, 1985: Three-dimensional flow in the upper ocean. *Science*, **227**, 1552–1556, doi:10.1126/science.227.4694.1552.

Zedel, L., and D. Farmer, 1991: Organized structures in subsurface bubble clouds: Langmuir circulation in the open ocean. *J. Geophys. Res.*, **96**, 8889–8900, doi:10.1029/91JC00189.